Sb-5*s* lone pair dynamics and collinear magnetic ordering in $Ba_2FeSbSe_5$

Stefan Maier,[1,*,‡] Michael W. Gaultois,[2] Nami Matsubara,[1,†] Wesley Surta,[3] Francoise Damay,[4] Sylvie Hebert,[1] Vincent Hardy,[1] David Berthebaud,[5] and Franck Gascoin[1,§]

[1]*Laboratoire CRISMAT UMR 6508 CNRS ENSICAEN, 6 boulevard du Maréchal Juin, 14050 Caen Cedex 04, France*

[2]*Leverhulme Research Centre for Functional Materials Design, The Materials Innovation Factory, Department of Chemistry, University of Liverpool, 51 Oxford Street, Liverpool L7 3NY, United Kingdom*

[3]*University of Liverpool, Department of Chemistry, Crown Street, Liverpool L69 7ZD, United Kingdom*

[4]*Laboratoire Léon Brillouin, CEA, Centre National de la Recherche Scientifique, CE-Saclay, 91191 Gif-sur-Yvette, France*

[5]*CNRS-Saint Gobain-NIMS, UMI 3629, Laboratory for Innovative Key Materials and Structures (LINK), National Institute for Materials Science, Tsukuba 305-0044, Japan*

(Received 17 April 2020; accepted 12 February 2021; published 25 February 2021)

Neutron diffraction and x-ray pair distribution function experiments were performed to investigate the magnetic and local crystal structures of $Ba_2FeSbSe_5$ and to compare them with the average (i.e., long range) structural model previously obtained by single-crystal x-ray diffraction. Changes in the local crystal structure (i.e., in the second coordination sphere) are observed upon cooling from 295 to 95 K, resulting in deviations from the average (i.e., long range) crystal structure. In this paper, we demonstrate that these observations cannot be explained by local or long-range magnetoelastic effects involving Fe-Fe correlations. Instead, we found that the observed differences between local and average crystal structure can be explained by Sb-5*s* lone pair dynamics. We also find that, below the Néel temperature ($T_N = 58$ K), the two distinct magnetic Fe^{3+} sites order collinearly, such that a combination of antiparallel and parallel spin arrangements along the *b* axis results. The nearest-neighbor arrangement ($J_1 = 6$ Å) is fully antiferromagnetic, while next-nearest-neighbor interactions are ferromagnetic in nature.

DOI: 10.1103/PhysRevB.103.054115

I. INTRODUCTION

Recently, Wang *et al.* discovered $Ba_2FeSbSe_5$ [1]. Further studies of this compound then led to the discovery of rapid phase changes between an amorphous and a crystalline phase upon laser irradiation [2], which is of significant interest for phase-change applications. It has been proposed that the structural distortions around the antimony atoms due to stereoactive Sb-5*s* lone pairs play an important role in understanding the interaction of the sample surface with pulsed laser light. These findings sparked interest in studying these structural distortions in more detail. In this context, this paper focuses on two aspects: magnetoelastic effects and Sb-5*s* lone pair stereoactivity. Figure 1 shows the crystal structure of $Ba_2FeSbSe_5$, including the connectivity of the $SbSe_6$ and $FeSe_4$ polyhedrons, as well as the stereoactivity of the Sb-5*s* lone pairs in Figs. 1(c) and 1(d). A second aspect of this paper focuses on the magnetic structure of $Ba_2FeSbSe_5$ to rule out magnetoelastic effects involving changes in the Fe-Fe distances at 95 K and to lay the foundation for a better understanding of the previously observed phonon-mediated coupling between magnetic spins and electric dipoles at the Néel temperature (58 K) [3], which is of significant interest for magnetodielectric technologies such as spin-charge transducers. The potential of $Ba_2FeSbSe_5$ as a magnetodielectric material, the diverse connectivity of the $FeSe_4$ tetrahedrons and $SbSe_6$ octahedrons (cf. Fig. 1), and different Fe-Fe distances also promise interesting arrangements and a complex magnetic coupling of the iron spins. Hence, neutron diffraction and x-ray pair distribution function (XPDF) experiments were carried out to gain a deeper understanding of the structural distortions in $Ba_2FeSbSe_5$, which helps understanding the observed phase-change and magnetodielectric properties of this remarkable semiconductor.

II. EXPERIMENTS

A. Heat capacity measurements

Heat capacity measurements were carried out in a Physical Properties Measurements System (PPMS, Quantum Design) by using a relaxation method with a 2τ analysis [4].

B. XPDF: experiments and data analysis

All experiments were conducted at the I15-1 XPDF beamline at the Diamond Light Source (Didcot, UK) using a focused x-ray beam (20 μm in size) with a wavelength of 0.16 Å. Two-dimensional x-ray scattering datasets were

*Present address: Institute of Physics IA, RWTH Aachen University, 52074 Aachen, Germany

†Present address: KTH Royal Institute of Technology, SE-100 44, Stockholm, Sweden

‡Corresponding author: s.maier@physik.rwth-aachen.de

§Corresponding author: franck.gascoin@ensicaen.fr

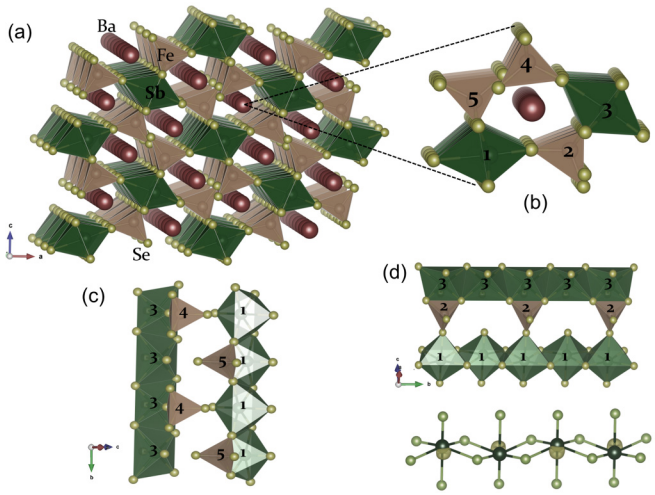

FIG. 1. (a) Crystal structure of $Ba_2FeSbSe_5$ (the unit cell is shown in Fig. S1 in the Supplemental Material [10]); (b) local Ba environment; (c) and (d) show differently connected chainlike fragments within the Fe-Sb-Se network; (d) also shows the local distortions of the $SbSe_6$ octahedrons due to stereoactive lone pairs. Sb: green, Fe: brown, Se: light green, Ba: red.

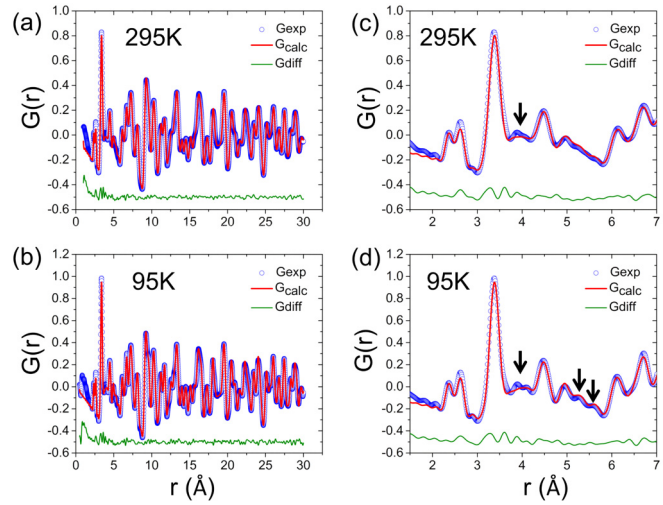

FIG. 2. Calculated (red) and experimental (blue) pair distribution functions (PDFs) with the corresponding difference plot (green) of crystalline $Ba_2FeSbSe_5$ at (a) 295 K and (b) 95 K; (c) and (d) show the low r range of the PDFs illustrating the changes in the local crystal structure upon cooling (cf. black arrows). All fits are based on a structural model, which represents the average (i.e., long range) atomic structure previously obtained from single-crystal x-ray diffraction experiments (cf. Ref. [1]).

recorded up to a momentum transfer of 36 $Å^{-1}$. Densely packed, 0.7-mm borosilicate capillaries were prepared before data collection. The capillaries were placed horizontally on a 10 Hz capillary spinner, and all samples were constantly rotated during data collection.

The beamline is equipped with a Bent-Laue monochromator (700 μm horizontal focusing), a multilayer mirror (20 μm vertical focusing), and a Perkin Elmer XRD1611 CP3 area detector with an active area of 409.6 × 409.6 mm^2. Data were collected at 295 and 95 K to increase the resolution by minimizing thermal vibrations. Low-temperature experiments were performed using a Cryojet operating with liquid nitrogen. The DAWN [5,6] software was used for data processing, and PDFget X_3 [7] was used to convert one-dimensional (1D) x-ray powder diffraction data to atomic pair distribution functions (PDFs). PDFfit2 was used to fit the experimental PDFs, and PDFgui was used as a graphical user interface [8]. LaB_6 was used to extract the Q_{damp} and Q_{broad} parameters used for all subsequent refinements. All refinements were performed refining the scale factor, lattice parameters, delta1 [accounts for the correlated motion of atoms at low r, which sharpens the first peak(s) at low r], thermal displacement parameters, and atomic positions. The thermal displacement parameters were constrained in a way so that $U_{11} = U_{22} = U_{33}$, and all U of the same atom type were assumed to be identical. Simultaneous fits of the PDF data and the reduced structure function [$F(Q)$] using large box models was done using the reverse Monte Carlo (RMC) method implemented in the RMCProfile software package [9]. Starting configurations were generated using Rietveld refinements from this paper at the corresponding temperatures. Supercells with lattice parameters of $7a \times 7b \times 7c$ consisting of 12 348 atoms were generated and fit using distance window constraints generated by analyzing structures from Rietveld refinements. Data were fit using a 1% tolerance on distance windows for interatomic distances for 24 h, followed by a 50% tolerance for 36 h. Simulations were run for 24 h, and all distance windows for all pair correlations were removed except for Fe-Se (1.15–2.55 Å) and Sb-Se (2.45–9 Å), allowing them to fit the full breadth of low-r pair correlations but preventing overfitting. Finally, data were fit within five runs (see Table S2 in the Supplemental Material [10]) with no constraints or restraints to ensure persistence of the final configuration.

C. Neutron powder diffraction

Temperature-dependent neutron powder diffraction (NPD) experiments were performed on the G4.1 beamline (CEA-Saclay, France, $\lambda = 2.426$ Å) within a temperature range of 1.5–300 K. Symmetry analysis and Rietveld refinements were performed using the FullProf Suite [11]. The former was carried out using the Bilbao Crystallographic Server [12,13].

III. RESULTS AND DISCUSSION

A. Signature of Sb-5*s* lone pair dynamics in the XPDF

XPDF data were recorded at the I15-1 XPDF beamline at the Diamond Light Source (Didcot, UK). Two datasets were recorded at 295 and 95 K (which is the lowest reachable temperature with this experimental setup) to increase the resolution by minimizing thermal vibrations. Figure 2 shows the experimental PDFs with the corresponding fits based on the structural model (space group: *Pnma*) of the average (i.e., long range) crystal structure obtained from single-crystal diffraction experiments performed by Wang *et al.* [1].

In general, the calculated and experimental PDFs agree quite well. A closer inspection of the low r range (i.e., from 2 to 7 Å), however, revealed clear misfits and changes in the atomic correlations between 3.8 and 5.6 Å upon cooling [cf.

Figs. 2(c) and 2(d)]. More specifically, we observe a peak splitting at approximately 4 Å and the sharpening of features at 5.3 and 5.6 Å. These features are not well described by the small box model (space group: *Pnma*) based on the average structural model obtained by Wang *et al.* [1].

With this paper, we demonstrate that these observations are signatures of Sb-5*s* lone pair dynamics. A detailed discussion in the Supplemental Material [10] will help convince the critical reader that these observations are not a result of measurement artifacts such as the termination of the diffraction data at finite momentum transfer (i.e., $Q_{\max} = 36\,\text{Å}^{-1}$) [14]. It has previously been shown [2] that a stereoactive lone pair electron density is localized at the Sb atoms, which results in a distorted octahedral arrangement of the Se atoms surrounding Sb [cf. Fig. 1(d)]. In the following, we will demonstrate that the peak splitting at $r \approx 4\,\text{Å}$ [cf. Fig. 1(d)] is a clear signature of this Sb-5*s* lone pair effect involving Sb-Se and Se-Se correlations. At 295 K, these are not as pronounced. There can be two reasons for this: (a) the resolution is not high enough to resolve the subtle differences in the Sb-Se and Se-Se correlations at 295 K due to thermal broadening, or (b) the $SbSe_6$ locally appear undistorted (i.e., the Sb-5*s* lone pairs are rather spherical) due to thermal vibrations of the atoms and can therefore not be resolved. In the following, we will demonstrate that the differences we observe in our PDF data between local and average (i.e., long range) crystal structure involve Sb-5*s* lone pair dynamics. To remove any ambiguity from the interpretation of our observations, it is required to rule out any magnetoelastic effects related to the iron spins, which is done in the next section.

B. Ruling out magnetoelastic effects due to local magnetic pre-ordering of the Fe spins

We previously found a coupling between phonons, magnetic spins, and electric dipoles at the Néel temperature (cf. Ref [3]), which is equivalent to magnetoelastic effects since electric dipoles can only form when the atoms are moving out of their equilibrium position, which happens at the same time as the magnetic spins are ordering. It is therefore necessary to rule out any magnetoelastic effects (i.e., changes in Fe-Fe distances due to short-range magnetic pre-ordering of the iron spins) at 95 K. It is important to keep in mind that macroscopic properties such as heat capacity (c_p) and magnetic susceptibility (χ) will only be influenced significantly by long-range magnetoelastic effects. This can be seen from Fig. 3, which shows the heat capacity (c_p) and magnetic susceptibility (χ) as a function of temperature (a zero-field cooled vs field cooled comparison for $\chi(T)$ can be found in the Supplemental Material [10]). The $\chi(T)$ and $c_p(T)$ curves show only one transition at the Néel temperature ($T_N = 58\,\text{K}$), which is consistent with previous reports on the magnetic properties of $Ba_2FeSbSe_5$ [1,3]**.** Hence, from a macroscopic point of view, there are no long-range magnetoelastic effects occurring between 295 and 95 K, which would cause changes in χ and c_p due to long-range magnetic ordering.

There is, however, the possibility of local magnetic pre-ordering (accompanied by a slight change in the Fe-Fe distances) or Se-mediated magnetic super exchange between the Fe atoms. Both scenarios do not result in long-range magnetic ordering and could be missed by only looking at macroscopic properties such as magnetic susceptibility and the heat capacity. To rule out local magnetoelastic effects involving changes in the Fe-Fe distances at 95 K, we compared structural models obtained from neutron diffraction and PDF data. It is important to note that we compare the average (i.e., long range) crystal structure (i.e., only the nuclear part in the fully ordered state) obtained from neutron diffraction and PDF data. Before doing so, it is necessary to obtain a model of the long-range ordered nuclear and magnetic structure from neutron diffraction data.

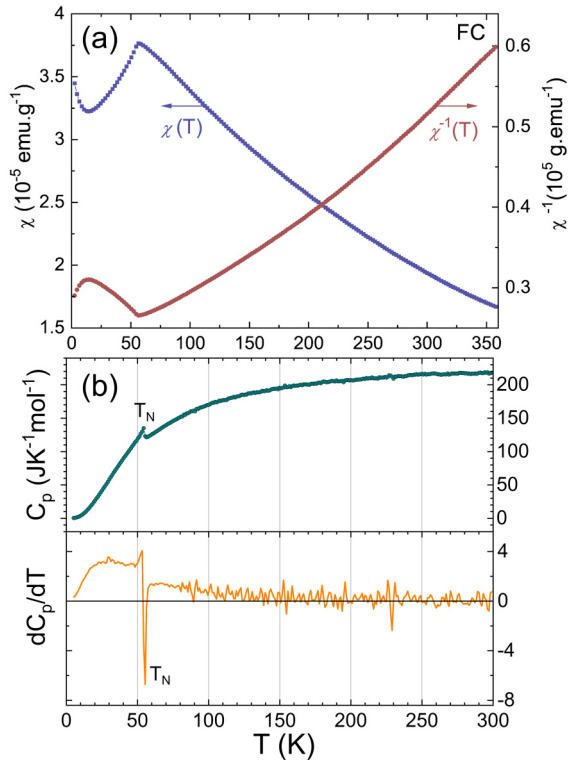

FIG. 3. (a) Magnetic susceptibility $\chi(T)$ of $Ba_2FeSbSe_5$ as a function of temperature and (b) top channel: heat capacity (c_p) and bottom channel: dc_p/dT showing only one transition corresponding to long-range magnetic ordering in crystalline $Ba_2FeSbSe_5$ below T_N. Hence, no long-range magnetoelastic effects can be observed between 300 and 95 K. The magnetic moment obtained from (a) is $6.8\,\mu_B$.

NPD experiments were carried out between 1.5 and 300 K. Figure 4(a) shows the temperature evolution of the NPD patterns, which confirms the long-range magnetic ordering below 58 K, manifesting itself in the appearance of additional Bragg reflections. The temperature evolution of the lattice parameters can be found in Fig. S3 in the Supplemental Material [10].

All the magnetic Bragg reflections can be indexed with the commensurate propagation vector $\mathbf{k} = (\frac{1}{2}\ 0\ \frac{1}{2})$, as can be seen from Fig. 4(c). To constrain the number of solutions for the magnetic model, a symmetry analysis was carried out for the Fe Wyckoff site 4*e*. There are eight irreducible representations with one dimension, each containing either 1 or 2 basis vectors. The best agreement between experimental data

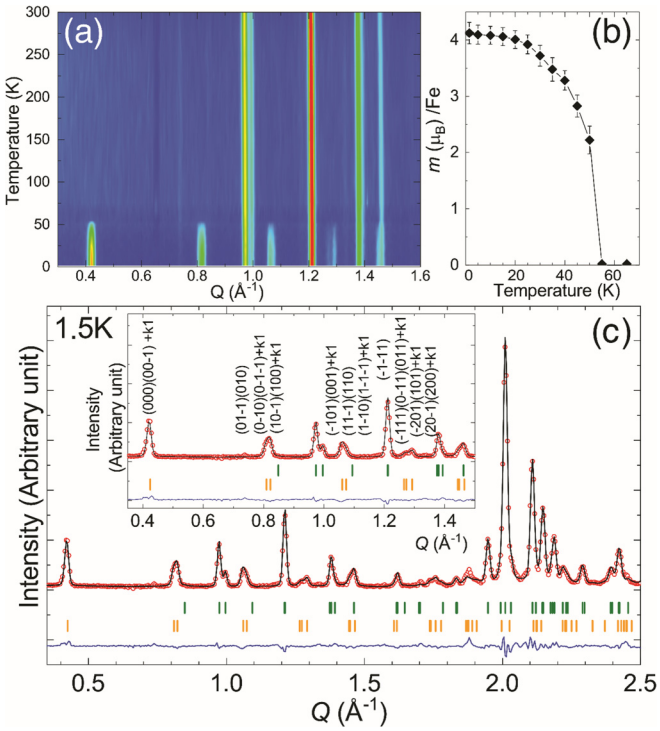

FIG. 4. (a) Neutron powder diffraction (NPD) patterns as a function of temperature showing magnetic reflections appearing below T_N; (b) magnetic moment (constrained) of Fe as a function of temperature; (c) Rietveld refinement ($R_{wp} = 4.58\%$, background corrected $R_{wp} = 9.93\%$, magnetic $R = 7.59\%$) of the diffraction pattern recorded at 1.5 K including the crystal and magnetic model; experimental data: open red circles; calculated profile: black continuous line; allowed Bragg reflections of the crystal (i.e., nuclear) and magnetic structure: green and orange vertical marks, respectively. The difference between the experimental and calculated profiles is displayed at the bottom of the graph as a blue continuous line. Please note that the neutron diffraction profiles of the crystal structure are based on a structural model describing the average (i.e., long range) atomic arrangement, which makes them comparable with the pair distribution function (PDF) model (cf. Fig. 5).

and our model is obtained for the Γ_4 and Γ_8 representations, whose basis vectors are summarized in Table I.

Both irreducible representations result in the Shubnikov group P_a2_1/m (#11.55), which has two independent, magnetic Fe sites within this magnetic symmetry. Only one magnetic component m_y can be refined independently. However, a magnetic model where only one out of two Fe sites is magnetically ordered results in a magnetic moment that is slightly too high ($\sim$5.8 μ_B) for an Fe^{3+} state with $S = \frac{5}{2}$ (expected 5 μ_B) and is unphysical. Thus, the magnetic moment of both iron sites was constrained to be the same since they are crystallographically identical. For data recorded at 1.5 K, the Rietveld refinement yields $m_y = 4.13\,(4)\,\mu_B$, which is close to the expected value of 5 μ_B for an Fe^{3+} state with $S = \frac{5}{2}$ and to the experimental moment of 5.3 μ_B found by Wang *et al.* [1]. The temperature evolution of the refined magnetic moment is depicted in Fig. 4(b). The magnetic moment obtained from our magnetic susceptibility data (cf. Fig. 3 and Fig. S4 in the Supplemental Material [10]) is slightly higher (i.e., 6.8 μ_B). A more detailed discussion concerning this point can be found in the Supplemental Material [10]. The model we obtain is a collinear magnetic structure with magnetic moments pointing along the b axis of the crystal structure (cf. Fig. 5). The magnetic structure can be visualized as two distorted triangular Fe^{3+} ladders running along the a and b axes [cf. Fig. 5(a)] with Fe-Fe distances ranging from 6.0 to 9.1 Å. Within the triangular ladders along the b axis, the nearest-neighbor arrangement (J_1 at a distance of 6.0 Å) can be understood as a zig-zag antiferromagnetic pattern [cf. gray, dotted line in Fig. 5(a)], whereas J_3 and J_4 correspond to ferromagnetic interactions [cf. thin green line in Fig. 5(a)]. The ladders running along the a axis can be described as two antiferromagnetic chains (J_2 at distance of 6.5 Å), which have an up-up-down-down spin structure resulting in geometrical frustration. $Ba_2FeSbSe_5$ shows antiferromagnetic ordering ($\Theta = -133\,(2)$ K) and a rather high transition temperature ($T_N = 58$ K), despite the rather large Fe-Fe distances (>6.0 Å). Similar spin arrangements were observed in antiperovskite chalcohalides such as $Ba_3(FeS_4)Br$, which also consists of FeS_4^{5-} tetrahedrons [15]. In this case, the shortest Fe-Fe distances are 6.2 Å, i.e., like those found in $Ba_2FeSbSe_5$, and yet a clear antiferromagnetic spin arrangement has also been observed for $Ba_3(FeS_4)Br$.

The magnetic interaction between the Fe atoms was rationalized by a Fe-S-S-Fe super exchange with a strong hybridization between the Fe d orbitals and the S p orbitals. The J_1 interaction in $Ba_2FeSbSe_5$ can be explained in an analog way by a Fe-Se-Se-Fe super exchange, which will be discussed further in the next section.

After establishing the model for the magnetic structure of $Ba_2FeSbSe_5$ at 1.5 K, we now compare the nuclear part with the local crystal structure obtained from our PDF data. The main focus lies on the Fe-Fe correlations to draw conclusions with respect to a local magnetoelastic coupling within the triangular framework involving a displacement of the Fe atoms, as it has been reported for $AgCrS_2$, $CuMnO_2$, $CuCrO_2$, and $NaMnO_2$ [16–18]. From Table S1 in the Supplemental Material [10] and from Figs. 5(c) and 5(d), it is clear that the local Fe-Fe correlations do not change upon cooling (slight

TABLE I. Irreducible representations (Γ_4 and Γ_8) for the 4*e* Fe site in the space group *Pnma* with $\boldsymbol{k} = (\frac{1}{2},\ 0,\ \frac{1}{2})$.

Irreducible representations		x, y, z	$-x+\frac{1}{2}, -y+1, z+\frac{1}{2}$	$-x+1, y+\frac{1}{2}, -z+1$	$x+\frac{1}{2}, -y+\frac{1}{2}, -z+\frac{1}{2}$
Γ_4	Re	0 1 0	0 0 0	0 −1 0	0 0 0
	Im	0 0 0	0 1 0	0 0 0	0 −1 0
Γ_8	Re	0 1 0	0 0 0	0 −1 0	0 0 0
	Im	0 0 0	0 −1 0	0 0 0	0 1 0

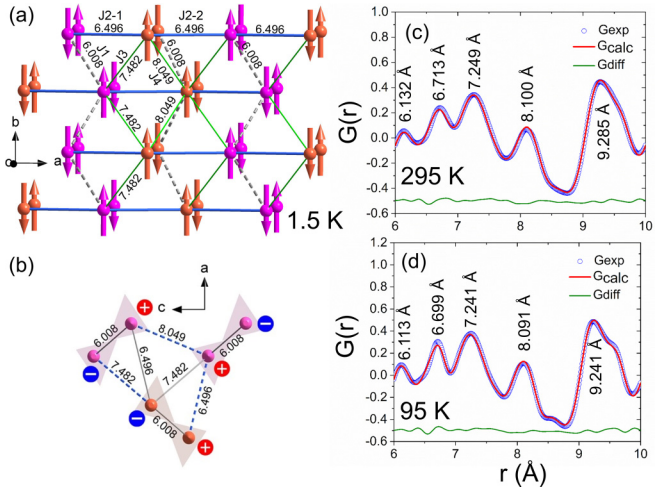

FIG. 5. Projections of the magnetic structure of $Ba_2FeSbSe_5$ in the (a) *a*-*b* plane and (b) in the *a*-*c* plane based on the refinement shown in Fig. 4. Two independent, magnetic Fe^{3+} sites—orange (Fe1) and pink (Fe2)—are distinguished in each projection. Fe-Fe distances in the triangular ladders are indicated; (c) and (d) Calculated (red) and experimental (blue) pair distribution functions (PDFs) showing the *r* range of the Fe-Fe correlations at 295 and 95 K, respectively. No misfits or changes in these correlations is visible, i.e., there are no differences between this part of the local and average crystal structure unlike those found for the Se-Se correlations depicted in Fig. 6. Please note that both the calculated PDF and neutron diffraction profiles of the atomic structure are based on a structural model describing the average (i.e., long range) atomic arrangement, which makes them comparable. The interatomic distances shown in (a) and (b) were extracted from our neutron powder diffraction (NPD) model obtained at 1.5 K (cf. Fig. 4 and Table S1 in the Supplemental Material [10]), while those depicted in (b) correspond to the PDF peak positions (i.e., the pairwise correlations). Slight differences in these interatomic distances are natural due to thermal expansion (cf. Table S1 in the Supplemental Material [10]).

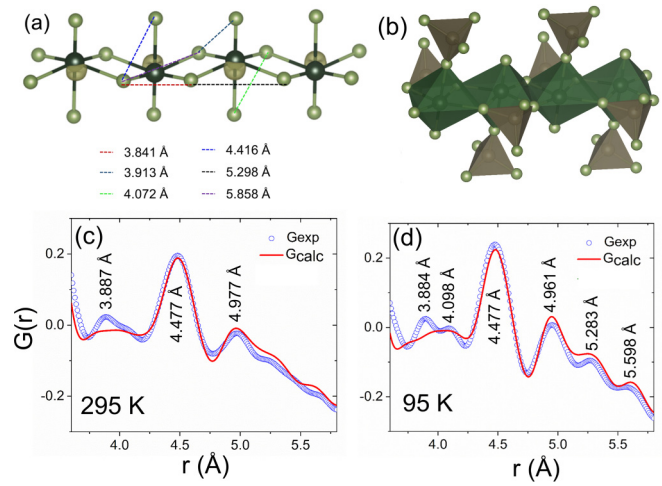

FIG. 6. (a) Local distortions of the $SbSe_6$ octahedrons due to stereoactive lone pairs (yellow) with the corresponding distances from the average crystal structure obtained by Wang *et al.*[1]; (b) connectivity of the $SbSe_6$ octahedrons and the $FeSe_4$ tetrahedrons. Calculated (red) and experimental (blue) pair distribution functions (PDFs) in the *r* range of the Se-Se correlations at (c) 300 K and (d) 95 K. Misfits between the calculated (i.e., average crystal structure) and the experimental PDFs (i.e., local crystal structure) as well as changes in the local crystal structure upon cooling are clearly visible. Please note that the interatomic distances depicted in (c) and (d) correspond to the peak position of the pairwise correlations obtained from the experimental PDF data. Slight differences between these interatomic distances and the ones shown in (a) are due to thermal expansion and the use of different experimental methods. However, the accuracy of all interatomic distances is sufficient to conclude that Sb-5*s* lone pair dynamics cause the observed peak splitting at approximately 4 Å and the sharpening of the PDF features at 5.3 and 5.6 Å. A comparison of all relevant interatomic distances can be found in Table S1 in the Supplemental Material [10].

changes due to thermal expansion are natural), and the average structural model describes these correlations well. Hence, both local and long-range magnetoelastic effects connected to changes in the Fe-Fe correlations cannot be observed by the experimental methods employed here. They can therefore be ruled out as being the origin of the observed differences between local and average (i.e., long range) crystal structure in the PDF data. Se-mediated Fe-Se-Se-Fe super exchange between the Fe atoms, however, cannot be ruled out, which is discussed in the next section.

C. Sb-5*s* lone pair dynamics vs Se-mediated magnetic super exchange

There is a series of studies which contributed to the understanding of local cation off-centering in inorganic or hybrid organic-inorganic solids [19–29]. All these publications demonstrated how powerful XPDF analyses and experiments are when investigating differences between average (i.e., long range) and local crystal structure. In this section, we discuss the observed peak splitting at approximately 4 Å and the sharpening of PDF features at 5.3 and 5.6 Å upon cooling in the context of two phenomena which are difficult (if not impossible) to disentangle in the case of $Ba_2FeSbSe_5$: Sb-5*s* lone pair dynamics and Se-mediated magnetic super exchange. Figures 6(c) and 6(d) show the experimental and calculated PDFs in the *r* range of the Sb-Se and Se-Se correlations (cf. Fig. 7), which surround the asymmetrically coordinated antimony atoms [cf. Fig. 6(a)]. It is important to note that the $SbSe_6$ octahedrons are connected to the $FeSe_4$ tetrahedrons via edges and corners [cf. Figs. 6(a) and 6(b)], i.e., Se-mediated magnetic super exchange as well as lone pair dynamics must be considered as possible origins of the observed changes in the local crystal structure of $Ba_2FeSbSe_5$. However, no experimental evidence of such effects was found, which would be visible as subtle changes in the Fe-Fe correlations resulting in differences between local and average crystal structure.

RMC simulations were performed to better describe the experimental PDF data in the area, where the local and average crystal structure differ and where changes in the PDFs with temperature are observed. Figures 7(a) and 7(b) show the improved model of the local crystal structure at 295 and 95 K, also describing the *r* range of the Sb-Se and Se-Se pair correlations well (the model for the entire experimental *r* range can be found in Fig. S7 in the Supplemental

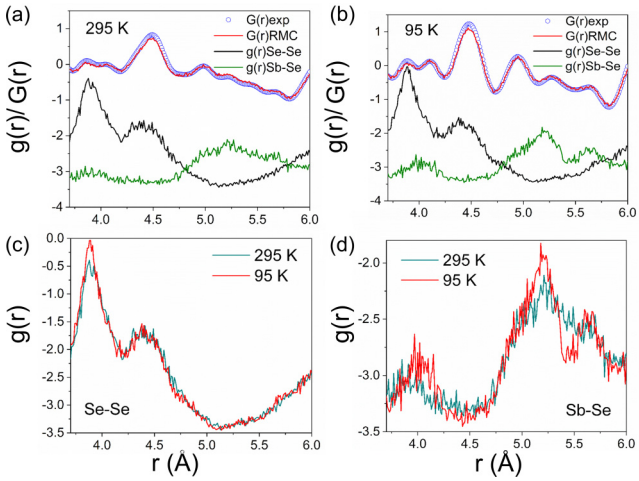

FIG. 7. Reverse Monte Carlo (RMC) fits of the experimental pair distribution function (PDF) data at (a) 295 K and (b) 95 K with the corresponding Sb-Se and Se-Se pair correlations. The RMC simulations result in a better description of the experimental data, which (due to Sb-5*s* lone pair effects) cannot be well described by the average structural model in the region of the Sb-Se and Se-Se correlations; (c) and (d) show subtle changes in the Sb-Se and Se-Se pair correlations with temperature. This figure provides evidence for Sb-5*s* lone pair dynamics being responsible for subtle differences between average and local crystal structure.

Material [10]). They also include the respective contributions of the Sb-Se and Se-Se pair correlations, while Figs. 7(c) and 7(d) depict the corresponding changes in Sb-Se and Se-Se pair correlations with temperature, where thermal broadening effects (i.e., changes in anisotropic displacement parameters) must be kept in mind. However, this figure provides strong evidence for Sb-5*s* lone pair dynamics being responsible for subtle differences between average and local crystal structure.

It is important to note that thermal broadening is an effect affecting all pairwise correlations (e.g., Fe-Fe). However, the small box model based on the average structural model obtained by Wang *et al.* only fails to describe the *r* range of the Sb-Se and Se-Se pair correlations adequately. This provides further evidence that what we observe in the XPDF data is an experimental signature of Sb-5*s* lone pair dynamics locally changing the Sb-Se and Se-Se correlations with respect to the average (i.e., long range) atomic arrangement. Hence, these findings strongly support the previous proposal that the structural distortions around the antimony atoms due to dynamic stereoactive lone pairs may play an important role in understanding the interaction of the sample surface with pulsed laser light [2]. However, further *in situ* XPDF experiments during laser irradiation are required to fully understand the amorphization process of $Ba_2FeSbSe_5$ when interacting with pulsed laser light.

IV. CONCLUSIONS

XPDF experiments revealed differences between average (i.e., long range) and local crystal structure as well as changes in the local crystal structure upon cooling from 295 to 95 K, which is well above $T_N = 58$ K. This paper demonstrates that these observations can be explained by Sb-5*s* lone pair dynamics locally changing the Sb-Se and Se-Se correlations and that these observations are not caused by local or long-range magnetoelastic effects involving Fe-Fe correlations. To rule out these effects, the crystal structure of the magnetically ordered phase was compared with the average crystal structure of the paramagnetic state (i.e., at 295 K). To make this comparison, a model of the magnetic structure below T_N (i.e., at 1.5 K) was obtained. The magnetic structure can be described as two distinct magnetic Fe^{3+} sites ordering collinearly, such that a combination of antiparallel and parallel spin arrangements along the *b* axis results. The nearest-neighbor arrangement ($J_1 = 6$ Å) is antiferromagnetic, while next-nearest-neighbor interactions are ferromagnetic.

ACKNOWLEDGMENTS

The authors acknowledge the Diamond Light Source for time on the I15-1 Beamline under the proposal EE16536 and particularly the support of Michael Wharmby during the beamtime. Furthermore, we acknowledge SOLEIL for providing NPD beamtime. Financial support from the French "Agence Nationale de la Recherche" (ANR) through the program "Investissements d'Avenir' (ANR-10-LABX-09-01), LabEx EMC3 is gratefully acknowledged.

[1] J. Wang, J. T. Greenfield, and K. Kovnir, Synthesis, crystal structure, and magnetic properties of quaternary iron selenides: $Ba_2FePnSe_5$ (Pn = Sb, Bi), J. Solid State Chem. **242**, 22 (2016).

[2] S. Maier, S. Hebert, H. Kabbour, D. Pelloquin, O. Perez, D. Berthebaud, and F. Gascoin, Synthesis, electronic structure and physical properties of polycrystalline $Ba_2FePnSe_5$ (Pn = Sb, Bi), Mater. Chem. Phys. **203**, 202 (2018).

[3] S. Maier, C. Moussa, D. Berthebaud, F. Gascoin, and A. Maignan, Coupled dielectric permittivity and magnetic susceptibility in the insulating antiferromagnet $Ba_2FeSbSe_5$, Appl. Phys. Lett. **112**, 202903 (2018).

[4] J. C. Lashley, M. F. Hundley, A. Migliori, J. L. Sarrao, P. G. Pagliuso, T. W. Darling, M. Jaime, J. C. Cooley, W. L. Hults, L. Morales, D. J. Thoma, J. L. Smith, J. Boerio-Goates, B. F. Woodfield, G. R. Stewart, R. A. Fisher, and N. E. Phillips, Critical examination of heat capacity measurements made on a Quantum Design physical property measurement system, Cryogenics **43**, 369 (2003).

[5] M. Basham, J. Filik, M. T. Wharmby, P. C. Y. Chang, B. El Kassaby, M. Gerring, J. Aishima, K. Levik, B. C. A. Pulford, I. Sikharulidze, D. Sneddon, M. Webber, S. S. Dhesi, F. Maccherozzi, O. Svensson, S. Brockhauser, G. Náray, and A. W. Ashton, Data analysis workbench (DAWN), J. Synchrotron Rad. **22**, 853 (2015).

[6] J. Filik, A. W. Ashton, P. C. Y. Chang, P. A. Chater, S. J. Day, M. Drakopoulous, M. W. Gerring, M. L. Hart, O. V. Magdysyuk, S. Michalik, A. Smith, C. C. Tang, N. J. Terrill, M. T. Wharmby,

and H. Wilhelm, Processing two-dimensional x-ray diffraction and small-angle scattering data in DAWN 2, J. Appl. Cryst. **50**, 959 (2017).

[7] P. Juhás, T. Davis, C. L. Farrow, and S. J. L. Billinge, PDFgetX3: a rapid and highly automatable program for processing powder diffraction data into total scattering pair distribution functions, J. Appl. Cryst. **46**, 560 (2013).

[8] C. L. Farrow, P. Juhás, J. W. Liu, D. Bryndin, E. S. Božin, J. Bloch, Th. Proffen, and S. J. L. Billinge, PDFfit2 and PDFgui: computer programs for studying nanostructure in crystals, J. Phys.: Condens. Matter. **19**, 335219 (2007).

[9] M. G. Tucker, D. A. Keen, M. T. Dove, A. L. Goodwin, and Q. Hui, RMCProfile: reverse Monte Carlo for polycrystalline materials, J. Phys.: Condens. Matter **19**, 335218 (2007).

[10] See Supplemental Material at http://link.aps.org/supplemental/10.1103/PhysRevB.103.054115 for Sb-5*s* lone pair dynamics and collinear magnetic ordering in $Ba_2FeSbSe_5$.

[11] J. Rodríguez-Carvajal, Recent advances in magnetic structure determination by neutron powder diffraction, Physica B Condens. Matter **192**, 55 (1993).

[12] M. I. Aroyo, J. M. Perez-Mato, C. Capillas, E. Kroumova, S. Ivantchev, G. Madariaga, A. Kirov, and H. Wondratschek, Bilbao crystallographic server: I. databases and crystallographic computing programs, Z. Cryst. **221**, 15 (2006).

[13] M. I. Aroyo, A. Kirov, C. Capillas, J. M. Perez-Mato, and H. Wondratschek, Bilbao crystallographic server. II. representations of crystallographic point groups and space groups, Acta. Cryst. A **62**, 115 (2006).

[14] Th. Proffen, S. J. L. Billinge, T. Egami, and D. Louca, Structural analysis of complex materials using the atomic pair distribution function—a practical guide, Z. Kristallogr. **218**, 132 (2003).

[15] X. Zhang, K. Liu, J.-Q. He, H. Wu, Q.-Z. Huang, J.-H. Lin, Z.-Y. Lu, and F.-Q. Huang, Antiperovskite chalco-halides $Ba_3(FeS_4)Cl$, $Ba_3(FeS_4)Br$ and $Ba_3(FeSe_4)Br$ with spin super-super exchange, Sci. Rep. **5**, 15910 (2015).

[16] F. Damay, C. Martin, V. Hardy, G. André, S. Petit, and A. Maignan, Magnetoelastic coupling and unconventional magnetic ordering in the multiferroic triangular lattice $AgCrS_2$, Phys. Rev. B **83**, 184413 (2011).

[17] A. V. Ushakov, S. V. Streltsov, and D. I. Khomskii, Orbital structure and magnetic ordering in stoichiometric and doped crednerite $CuMnO_2$, Phys. Rev. B **89**, 024406 (2014).

[18] M. Poienar, F. Damay, C. Martin, J. Robert, and S. Petit, Spin dynamics in the geometrically frustrated multiferroic $CuCrO_2$, Phys. Rev. B, **81**, 104411 (2010).

[19] G. Laurita, D. H. Fabini, C. C. Stoumpos, M. G. Kanatzidis, and R. Seshadri, Chemical tuning of dynamic cation off-centering in the cubic phases of hybrid tin and lead halide perovskites, Chem. Sci. **8**, 5628 (2017).

[20] M. Giot, L. C. Chapon, J. Androulakis, M. A. Green, P. G. Radaelli, and A. Lappas, Magnetoelastic Coupling and Symmetry Breaking in the Frustrated Antiferromagnet α-$NaMnO_2$, Phys. Rev. Lett. **99**, 247211 (2007).

[21] E. S. Božin, C. D. Malliakas, P. Souvatzis, T. Proffen, N. A. Spaldin, M. G. Kanatzidis, and S. J. L. Billinge, Entropically stabilized local dipole formation in lead chalcogenides, Science **330**, 1660 (2010).

[22] B. Sangiorgio, E. S. Božin, C. D. Malliakas, M. Fechner, A. Simonov, M. G. Kanatzidis, S. J. L. Billinge, N. A. Spaldin, and T. Weber, Correlated local dipoles in PbTe, Phys. Rev. Mater. **2**, 085402 (2018).

[23] K. M. Ø. Jensen, E. S. Božin, C. D. Malliakas, M. B. Stone, M. D. Lumsden, M. G. Kanatzidis, S. M. Shapiro, and S. J. L. Billinge, Lattice dynamics reveals a local symmetry breaking in the emergent dipole phase of PbTe, Phys. Rev. B **86**, 085313 (2012).

[24] K. R. Knox, E. S. Božin, C. D. Malliakas, M. G. Kanatzidis, and S. J. L. Billinge, Local off-centering symmetry breaking in the high-temperature regime of SnTe, Phys. Rev. B **89**, 014102 (2014).

[25] R. Yu, E. S. Božin, M. Abeykoon, B. Sangiorgio, N. A. Spaldin, C. D. Malliakas, M. G. Kanatzidis, and S. J. L. Billinge, Emphanitic anharmonicity in PbSe at high temperature and the anomalous electronic properties in the PbQ (Q = S, Se, Te) system, Phys. Rev. B **98**, 144108 (2018).

[26] H. Takenaka, I. Grinberg, and A. M. Rappe, Anisotropic Local Correlations and Dynamics in a Relaxor Ferroelectric, Phys. Rev. Lett. **110**, 147602 (2013).

[27] D. Hou, C. Zhao, A. R. Paterson, S. Li, and J. L. Jones, Local structures of perovskite dielectrics and ferroelectrics via pair distribution function analyses, J. Eur. Ceram. Soc. **38**, 971 (2018).

[28] G. Laurita, K. Page, S. Suzuki, and R. Seshadri, Average and local structure of the Pb-free ferroelectric perovskites (Sr,Sn)TiO_3 and (Ba,Ca,Sn)TiO_3, Phys. Rev. B **92**, 214109 (2015).

[29] M. Dutta, K. Pal, U. V. Waghmare, and K. Biswas, Bonding heterogeneity and lone pair induced anharmonicity resulted in ultralow thermal conductivity and promising thermoelectric properties in *n*-type $AgPbBiSe_3$, Chem. Sci. **10**, 4905 (2019).